Computational Materials Science 143 (2018) 325–337

Contents lists available at ScienceDirect

Computational Materials Science

journal homepage: www.elsevier.com/locate/commatsci

Residual stresses and distortion in additively manufactured compositionally graded and dissimilar joints

T. Mukherjee [a], J.S. Zuback [a], W. Zhang [b], T. DebRoy [a,*]

[a] Department of Materials Science and Engineering, The Pennsylvania State University, University Park, PA 16801, United States
[b] Department of Materials Science and Engineering, The Ohio State University, Columbus, OH 43221, United States

ARTICLE INFO

Article history:
Received 19 October 2017
Received in revised form 11 November 2017
Accepted 13 November 2017

Keywords:
Additive manufacturing
3D printing
Transition joint
Thermo-mechanical modeling
Finite element analysis
Thermodynamic calculations

ABSTRACT

Additively manufactured compositionally graded joints are potentially attractive to minimize abrupt changes in residual stresses and distortion of dissimilar alloy joints. Performance of these graded joints depends on the residual stresses and distortion governed by the transient temperature field during additive manufacturing and local mechanical properties of the joint. Here we develop, validate and utilize a thermo-mechanical model to provide a definitive way to additively manufacture sound graded joints for minimizing abrupt changes in residual stresses and distortion of the dissimilar joints. This model calculates residual stresses and distortion from accurate temperature fields calculated using a well-tested heat transfer and fluid flow model and temperature dependent alloy properties estimated by thermodynamic calculations. Both graded and dissimilar joints of 2.25Cr-1Mo steel to alloy 800H and Ti-6Al-4V to 800H, fabricated using laser-assisted powder based direct energy deposition process are examined. It is found that the sharp changes in residual stresses in dissimilar joints between Ti-6Al-4V and 800H can be effectively minimized by fabricating a graded joint between them. Although the magnitudes of residual stresses in Ti-6Al-4V to 800H joint are higher than that in 2.25Cr-1Mo steel to 800H joint, the former is less susceptible to warping, buckling and delamination due to the high room temperature yield strength of the Ti-6Al-4V substrate.

1. Introduction

Dissimilar metal joints are used in aerospace, nuclear power generation, marine and automobile industries [1,2]. However, dissimilar joints often fail because of the distortion and high gradient of residual stresses generated due to the sharp changes in chemical composition and properties across the joint interface [2–5]. These difficulties can be minimized by the development of compositionally graded transition joints where the variations of chemical composition and properties occur smoothly across the joint over a large distance [6,7]. Additive manufacturing (AM) is a practical choice to fabricate compositionally graded transition joints by adding materials of varying compositions in a layer-by-layer manner [8–12]. AM has already been used to fabricate transition joints between stainless steels and nickel base superalloys for nuclear applications [10,11] and between titanium alloys and iron-nickel alloys for aerospace applications [12]. However, additively manufactured compositionally graded components also encounter residual stresses and distortion because of the spatially non-uniform and transient temperature field during the process. Depending on the local room temperature yield strength of the graded components, these residual stresses and distortion may result in premature fatigue failure, delamination, warping and buckling. Therefore, accurate estimations of residual stresses and distortion are necessary for both dissimilar and graded joints to fabricate sound compositionally graded components by AM for minimizing abrupt change in residual stresses and distortion of the dissimilar joints.

There are two main differences in residual stresses and distortion between compositionally graded and single alloy components. First, the evolution of residual stresses depends on the cooling process of the component at the end of the deposition. In graded components, the difference in the thermo-physical properties between the two end alloys governs the cooling process and thus the evolution of the residual stresses and distortion. Second, susceptibilities to warping, buckling and delamination depend not only on the magnitudes of the residual stresses but also on the local room temperature yield strength of the graded component. Since, the yield strength varies spatially in many compositionally graded components, two regions with the same magnitude of residual stresses

* Corresponding author.
E-mail address: debroy@psu.edu (T. DebRoy).

https://doi.org/10.1016/j.commatsci.2017.11.026
0927-0256/

can have different susceptibilities to delamination, buckling and warping.

Experimental measurements of residual stresses and distortion of AM components are time consuming and expensive [13]. These measurements also depend on sample preparation, shape and size of the components and accuracy of the experimental methods such as X-ray or neutron diffraction [14–16]. For both compositionally graded and dissimilar metal joints, use of non-destructive measurement techniques are restricted by the limited availability of strain free lattice spacing for all compositions [4,17]. A recourse is to calculate residual stresses and distortion in all locations of the component using numerical models. However, most of the existing numerical models of AM residual stresses neglect the convective flow of liquid metal inside the molten pool that often dominates the heat transfer during AM [18]. This simplification may result in inaccuracy in temperature field calculations, [19] and as a result, residual stresses and strain calculated based on such inaccurate temperatures can become unreliable [18]. Another difficulty in these calculations is the limited availability of the temperature dependent thermo-physical and mechanical properties data for different alloy compositions used in the graded components [20]. In the literature, thermodynamic calculations have been done to estimate the alloy properties for graded joints between titanium alloys, nickel base superalloys and steels [11,12]. However, so far the estimated properties have not been used to calculate residual stresses and distortion of the compositionally graded transition joints. Because of the challenges mentioned above, literature on the estimation of residual stresses and distortion of additively manufactured compositionally graded components is scarce.

Here, we calculate, for the first time, the residual stresses and distortion of compositionally graded joints as well as dissimilar joints of (a) 2.25Cr-1Mo steel to an iron-nickel alloy (800H) and (b) a titanium alloy (Ti-6Al-4V) to 800H, fabricated using laser assisted powder based direct energy deposition process. In these graded joints, alloy composition changes with layers along the build height direction. A thermo-mechanical model is used to calculate residual stresses and distortion from the transient temperature field accurately estimated using a heat transfer and fluid flow model that considers the effects of convective flow of liquid metal. The temperature and composition dependent thermo-physical and mechanical properties are estimated by thermodynamic calculations using a commercial program, JMatPro®. This program calculates different alloy properties for a specified temperature range based on the chemical composition of the alloy. The thermo-mechanical model is rigorously tested and validated against independent experimental data. The spatial variation of the residual stresses and distortion for the two types of graded joints is compared based on their alloy properties, transient temperature fields and molten pool dimensions. The relative advantages of fabricating graded joints over dissimilar joints for minimizing the abrupt changes in residual stresses and distortion are examined for the two types of joints.

2. Theoretical investigation

2.1. Modeling assumptions

The calculations of the residual stresses and distortion are performed in two steps. First, a well-tested three-dimensional heat transfer and fluid flow model [21–23] is used to calculate transient temperature fields. Second, based on the calculated temperature fields, residual stresses and distortion are predicted using a commercial finite element analysis (FEA) code, Abaqus® [24]. The following simplified assumptions are made in both the heat transfer and fluid flow model and the FEA mechanical model.

(1) Densities of the solid and liquid alloys are considered as temperature independent.
(2) The surfaces of the deposited layers are assumed to be flat.
(3) The effects of strains induced by solid-state phase transformation and creep are neglected to make the calculations tractable.
(4) Each layer is assigned to a pre-defined composition and the effect of dilution due to re-melting of the substrate or previous layers on the layer composition is not considered.

2.2. Thermodynamic calculations for alloy properties

Temperature and composition dependent thermo-physical and mechanical properties of alloys are needed for the heat transfer and fluid flow calculations as well as the finite element based mechanical model. During the fabrication of compositionally graded joints, the mixing of chemistries often leads to high alloying element concentrations. Local chemical compositions can extend into regions where experimental property data are not available and approximations such as simplified phase diagrams, stress-strain plots and dilute alloy properties are not applicable. An alternative for determining important material properties is through numerical modeling based on elemental mixing interactions. JMatPro® is a thermodynamic program designed for materials processing applications that models important alloy properties such as equilibrium phases, phase transformations, thermo-physical properties and mechanical behavior [25]. The CALculation of PHAse Diagrams (CALPHAD) method, which is widely established in the literature [26], is used to determine phase fractions and compositions for a given alloy concentration and temperature or temperature range.

The modeling of thermo-physical and mechanical properties using JMatPro® involves the following sequential steps. First, the equilibrium fraction of phases is determined through the minimization of the total Gibbs energy method using thermodynamic excess functions to account for the mixing of elements. The property, P, of interest for each phase is expressed as [27],

$$P = \sum_i x_i P_i^0 + \sum_i \sum_{j>1} x_i x_j \sum_v \Omega_{ij}^v (x_i - x_j)^v \quad (1)$$

where P_i^0 is the property of the phase in the pure element, Ω_{ij}^v is a binary interaction parameter between elements i and j dependent on an integer, v. x_i and x_j are the mole fractions of i and j in the phase, respectively. The effects of temperature on the property of a phase are taken into account through both P_i^0 and Ω_{ij}^v, which are function of temperature. The total property of the alloy is then determined from the phase fractions and properties of each phase using the general law of mixtures [28]. The use of this type of model allows for the approximation of both thermo-physical and mechanical properties as functions of composition and temperature and accounts for effects of multi-phase microstructure. The thermo-physical and mechanical properties of different alloy compositions are provided in Tables 1–5 and in Supplementary document.

2.3. Governing equations and boundary conditions

Detailed description of the thermo-mechanical model is available in a previous publication [18]. For completeness, a few salient features of the model are provided as follows. The heat transfer and fluid flow model solves the equations of conservation of mass, momentum and energy [29], as given below, respectively.

$$\frac{\partial (\rho u_i)}{\partial x_i} = 0 \quad (2)$$

Table 1
Thermo-physical properties of SS 410, 2.25Cr-1Mo steel, Ti-6Al-4V and 800H. Here 'T' represents temperature in K.

Properties	SS 410	2.25Cr-1Mo steel	Ti-6Al-4V	800H
Liquidus temperature (K)	1749	1787	1928	1675
Solidus temperature (K)	1640	1740	1878	1608
Thermal conductivity (W/m K)	14.0 + 0.0125 T	11.82 + 0.0106 T	$1.57 + 0.016\ T - 1 \times 10^{-6}\ T^2$	8.54 + 0.0167 T
Specific heat (J/kg K)	$447.2 + 0.041\ T - 4.18 \times 10^{-6}\ T^2$	461.4 + 0.1338 T	$492.4 + 0.025\ T - 4.18 \times 10^{-6}\ T^2$	309.2 + 0.5104 T
Density (kg/m^3)	7160	7270	4000	7870
dγ/dT (N/m K)	-0.40×10^{-3}	-0.44×10^{-3}	-0.26×10^{-3}	-0.24×10^{-3}

Table 2
Temperature dependent mechanical properties of SS 410 in annealed condition.

Temperature (K)	Young's modulus (GPa)	Temperature (K)	Volumetric expansion co-efficient (/K)	Temperature (K)	Yield stress (MPa)
300	191.2	300	21.93E−06	300	284.0
400	183.6	400	22.07E−06	700	164.0
500	175.9	500	22.21E−06	1100	150.0
600	168.1	600	22.37E−06	1300	77.2
700	160.1	700	22.53E−06	1500	22.3
800	152.0	800	22.70E−06		
900	143.8	900	22.88E−06		
1000	135.5	1000	23.07E−06		
1100	127.0	1100	23.27E−06		
1200	118.1	1200	23.53E−06		
1300	108.4	1300	23.94E−06		
1400	99.7	1400	24.14E−06		
1500	89.6	1500	24.50E−06		
1640	59.5	1640	25.52E−06		

Table 3
Temperature dependent mechanical properties of 2.25Cr-1Mo steel.

Temperature (K)	Young's modulus (GPa)	Temperature (K)	Volumetric expansion co-efficient (/K)	Temperature (K)	Yield stress (MPa)
300	211.3	300	12.39E−06	300	312.5
400	206.4	400	12.76E−06	700	156.9
500	200.0	500	13.12E−06	1100	88.1
600	191.5	600	13.49E−06	1300	57.7
700	181.0	700	13.85E−06	1500	42.4
800	168.8	800	14.22E−06		
900	155.2	900	14.59E−06		
1000	140.4	1000	14.98E−06		
1100	124.2	1500	15.22E−06		
1200	109.1	1600	16.01E−06		
1300	98.3	1700	17.13E−06		
1400	81.36				
1500	61.31				
1600	34.12				
1700	8.79				

Table 4
Temperature dependent mechanical properties of Ti-6Al-4V.

Temperature (K)	Young's modulus (GPa)	Temperature (K)	Volumetric expansion co-efficient (/K)	Temperature (K)	Yield stress (MPa)
300	125	300	8.78E−06	300	955
533	110	533	9.83E−06	573	836
589	100	589	10.0E−06	773	732
700	93	700	10.7E−06	1023	581
755	80	755	11.1E−06	1073	547
811	74	811	11.2E−06	1173	480
923	55	923	11.7E−06	1273	405
1073	27	1073	12.2E−06	1373	330
1098	22	1098	12.3E−06		
1123	18	1123	12.4E−06		
1573	12	1573	13.0E−06		
1873	9	1873	16.3E−06		

$$\frac{\partial(\rho u_j)}{\partial t} + \frac{\partial(\rho u_j u_i)}{\partial x_i} = \frac{\partial}{\partial x_i}\left(\mu \frac{\partial u_j}{\partial x_i}\right) + S_j \quad (3)$$

$$\rho \frac{\partial h}{\partial t} + \frac{\partial(\rho u_i h)}{\partial x_i} = \frac{\partial}{\partial x_i}\left(\frac{k}{C_p}\frac{\partial h}{\partial x_i}\right) - \rho \frac{\partial \Delta H}{\partial t} - \rho \frac{\partial(u_i \Delta H)}{\partial x_i} \quad (4)$$

where ρ is the density, u_i and u_j are the velocity components along the i and j directions, respectively, and x_i is the distance along the i direction, t is the time, μ is the effective viscosity, and S_j is a source term for the momentum equation. h is the sensible heat, C_p is the specific heat, k is the thermal conductivity, and ΔH is the latent heat content.

Table 5
Temperature dependent mechanical properties of 800H.

Temperature (K)	Young's modulus (GPa)	Temperature (K)	Volumetric expansion co-efficient (/K)	Temperature (K)	Yield stress (MPa)
300	200.7	300	15.68E−06	300	272.3
400	194.5	400	16.01E−06	500	157.7
500	188.0	500	16.34E−06	700	139.3
600	181.3	600	16.68E−06	1500	50.8
700	174.4	700	17.02E−06		
800	167.3	800	17.35E−06		
900	158.8	900	17.71E−06		
1000	148.4	1000	18.18E−06		
1100	139.1	1100	19.10E−06		
1200	131.2	1200	19.47E−06		
1300	113.1	1300	19.85E−06		
1400	94.7	1400	20.24E−06		
1500	76.0	1500	20.65E−06		
1600	37.1	1600	21.05E−06		

The Abaqus® based finite element analysis (FEA) code solves the constitutive equations for elastic, plastic and thermal strains where the total strain increment ($\Delta\varepsilon_{lm}^{tot}$) with respect to time is represented as,

$$\Delta\varepsilon_{lm}^{tot} = \Delta\varepsilon_{lm}^{E} + \Delta\varepsilon_{lm}^{P} + \Delta\varepsilon_{lm}^{Th} + \Delta\varepsilon_{lm}^{V} \quad (5)$$

where $\Delta\varepsilon_{lm}^{E}$, $\Delta\varepsilon_{lm}^{P}$ and $\Delta\varepsilon_{lm}^{Th}$ are the elastic, plastic and thermal strain increments respectively. $\Delta\varepsilon_{lm}^{V}$ is the strain induced due to the solid state phase transformation and creep, which is assumed to be zero in the present model [18].

Convective and radiative heat losses to the surroundings [21,22] are applied on the walls of the deposit and the substrate as boundary conditions in heat transfer and fluid flow model. Liquid metal convection inside the molten pool driven by the spatial gradient of surface tension due to the temperature gradient on the top surface of the pool, known as Marangoni convection [23,30,31], governs the temperature distribution. To consider this effect in the calculation, Marangoni shear stress (τ) is applied as a boundary condition to calculate the velocities of the molten metal and is expressed as [30]:

$$\tau = \frac{d\gamma}{dT}\frac{dT}{dr} = \mu\frac{du}{dz} \quad (6)$$

where T is the temperature, u is velocity of the liquid metal on the top surface of the molten pool, γ is the surface tension, μ is the viscosity and r is the radial distance from the axis of the heat source. The boundary conditions for the FEA mechanical model include fixed bottom surface, i.e., the displacements of all nodes of the bottom surface along the x, y and z directions are zero.

2.4. Algorithm of the thermo-mechanical model

A Python script is utilized to export the mesh and the transient temperature fields from the heat transfer and fluid flow model to the Abaqus-based FEA model. This script creates a database file containing the nodes, elements and transient temperature fields using the Abaqus Scripting Interface. This database file is imported to the FEA mechanical model to calculate residual stresses, strain and distortion incorporating the temperature dependent mechanical properties estimated using JMatPro®. The detailed algorithm of the thermo-mechanical model is summarized in Fig. 1.

2.5. Utilization of the model for graded and dissimilar joints

In this research, two types of graded joints are considered, 2.25Cr-1Mo steel to 800H joint and Ti-6Al-4V to 800H joint. Substrates for these two graded joints are 2.25Cr-1Mo steel and

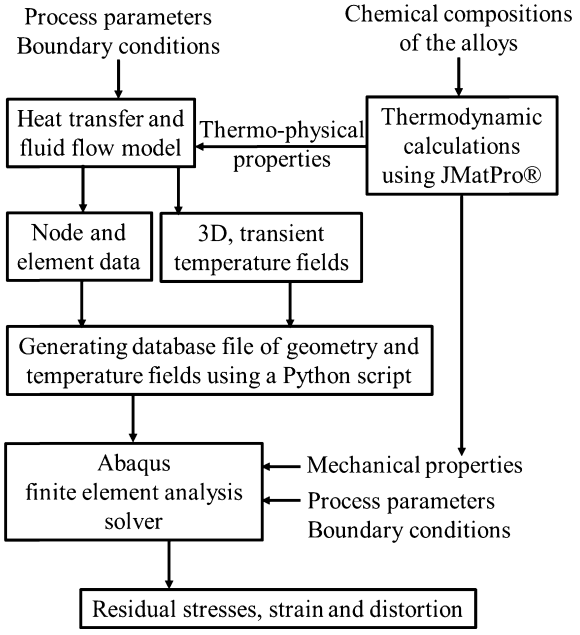

Fig. 1. Outline of the thermo-mechanical model combining the heat transfer and fluid flow model with the FEA mechanical model.

Ti-6Al-4V, respectively. For both joints, the 10th layer is made by 100% alloy 800H. From the 1st layer to the 9th layer, the composition is changed linearly with an increment of 10 wt% of 800H. For instance, the composition of the 1st layer is 10% 800H and 90% Ti-6Al-4V or 2.25Cr-1Mo steel and composition of the 9th layer is 90% 800H and 10% Ti-6Al-4V or 2.25Cr-1Mo steel. For the dissimilar joints, substrate and layer 1 to layer 5 are made of Ti-6Al-4V or 2.25Cr-1Mo steel and 6th to 10th layer are made of 800H. Therefore, sharp change in composition occurs at the interface of 5th and 6th layer of the dissimilar joints. Schematic representations of both graded and dissimilar joints are given in Fig. 2. For the purpose of model validation, a build-up of 10 layer, single pass wall made of entirely stainless steel 410 (SS 410) is also studied.

Fig. 3 represents the solution domain, and the detailed dimensions are provided in Table 6. Half of the solution domain is considered by taking advantage of the y-symmetry. The laser beam travels along the positive x-axis. The component is built vertically upward along the positive z-axis with the deposition of 10 layers. The residual stress along x-direction (σ_x) is referred as longitudinal stress and is primarily responsible for crack propagation, buckling and warping [18]. The through-thickness

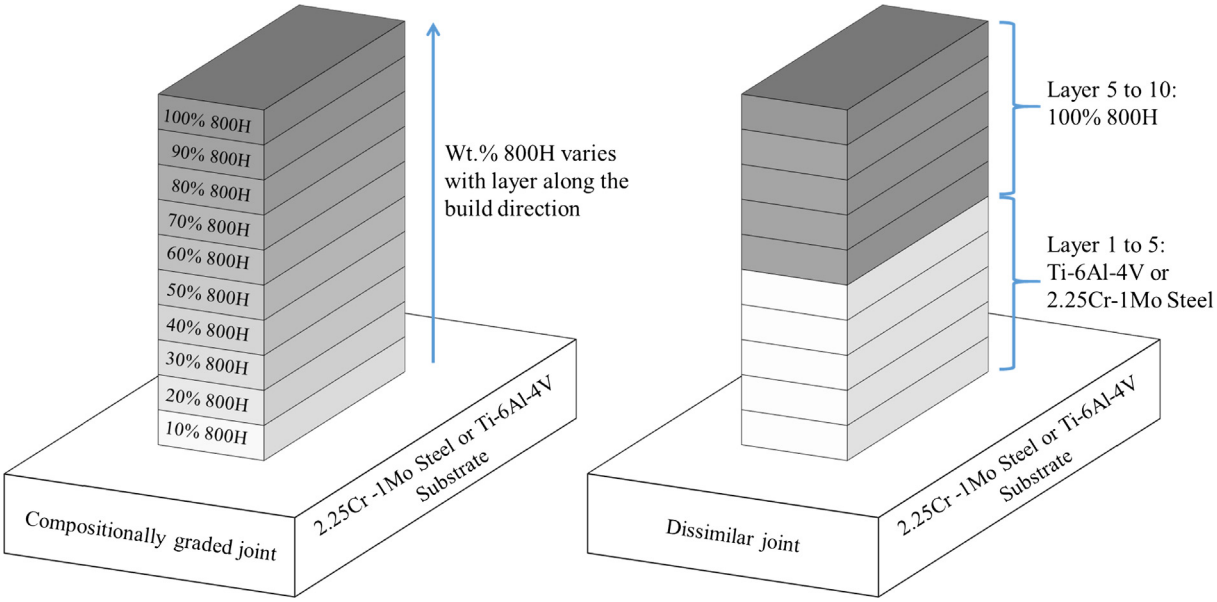

Fig. 2. Schematic representation of the compositionally graded and the dissimilar joints fabricated using additive manufacturing.

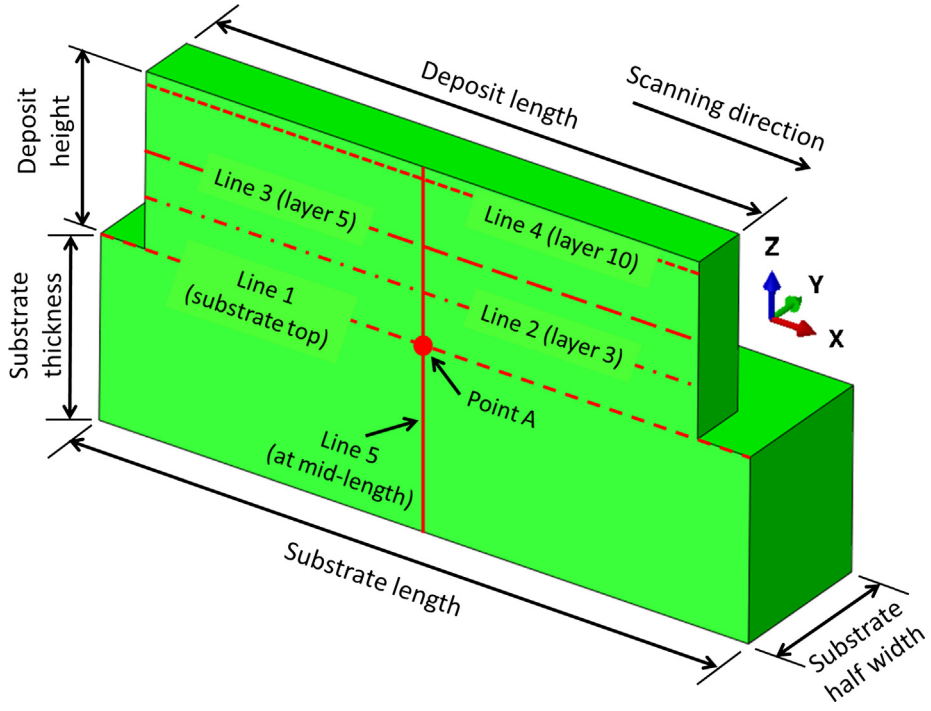

Fig. 3. Solution domain for the heat transfer and fluid flow calculations and the subsequent mechanical analysis. Due to the y-symmetry, a half of the solution domain is considered to reduce time and computer memory requirements for the analysis. The five lines along which residual stress values are surveyed and the one point at which temperature variation with time is monitored are shown. The values of the dimensions are provided in Table 6.

Table 6
Process parameters used for calculations.

Parameter set	Laser power (W)	Scanning speed (mm/s)	Powder flow rate (gm/s)	Deposit height (mm)	Deposit length (mm)	Substrate dimension (mm)
1	300, 600	2.5, 4.2	0.358	5	10	$10 \times 4 \times 1$
2	300	10	0.432	3.8	12	$14 \times 5 \times 4$

residual stress along z-direction (σ_z) may cause delamination and detachment of the component from the substrate [18]. Residual stress and strain distributions are spatially non-uniform depending on the local material properties. To capture this non-uniformity, residual stress distributions are plotted along five lines shown in Fig. 3.

3. Results and discussions

3.1. Model validation

Fig. 4 shows fair agreements between the calculated through-thickness residual stresses (σ_z) and the corresponding experimentally measured values [32] for a 10 layer laser-assisted SS 410 deposit. Fig. 4(a) and (b) shows the through-thickness residual stresses along 'line 2' (in Fig. 3) for two different scanning speeds and 300 W laser power. Through-thickness residual stresses along the 'line 5' (in Fig. 3) are plotted for two different scanning speeds and 600 W laser power in Fig. 4(c) and (d). Several measurements were taken to estimate the error bars as shown in Fig. 4. The slight mismatch between the experimental and calculated values could be caused by both the measurement difficulties and the assumptions used in numerical calculations. Validity of the numerical model provides us the confidence to apply the model for compositionally graded transition joints.

3.2. Temperature and velocity distributions in graded joints

Fig. 5 shows the temperature and velocity fields when the laser beam is at the mid-length of the deposit during the deposition of 1st, 5th and 10th layers. Fig. 5(a)–(c) and (d)–(f) are for 2.25Cr-1Mo steel to 800H joint and Ti-6Al-4V to 800H joint, respectively. The zones marked by red color and bounded by the liquidus temperature isotherm of the corresponding alloy, represent the fusion zone. The length of the fusion zones (molten pool length) are mentioned in the figures. The arrows shown in the figures represent the velocity vectors of the liquid metal inside the molten pool. The magnitude of the velocities can be read by comparing the length of these arrows with the length of the reference vector provided. In AM, most of the heat is transferred downwards through the substrate [33]. Therefore, during the deposition of the upper layers, heat transfer from the molten pool through the substrate decreases [33]. That results in larger molten pool for upper layers in 2.25Cr-1Mo steel to 800H joint as shown in Fig. 5(a)–(c). However, in Ti-6Al-4V to 800H joint, the density of 800H is almost twice than that of Ti-6Al-4V (see Table 1). Therefore, under the same processing conditions, Ti-6Al-4V exhibits larger molten pool than 800 H. Therefore, in Ti-6Al-4V to 800H joint, the molten pool size is decided by trading off two opposing factors, (1) reduction in pool size for upper layers due to increasing density from Ti-6Al-4V to 800H and (2) increase in pool size for upper layers due to reduced heat transfer through the substrate. As a result, the molten pool size does not change significantly as shown in Fig. 5(d)–(f).

3.3. Residual stresses and distortion in graded joints

These spatially non-uniform temperature and velocity fields, shown in Fig. 5, result in thermal distortion. For quantitative understanding of thermal distortion, we have recently proposed [34,35] a strain parameter (ε^*) as an indicator of the susceptibility to distortion.

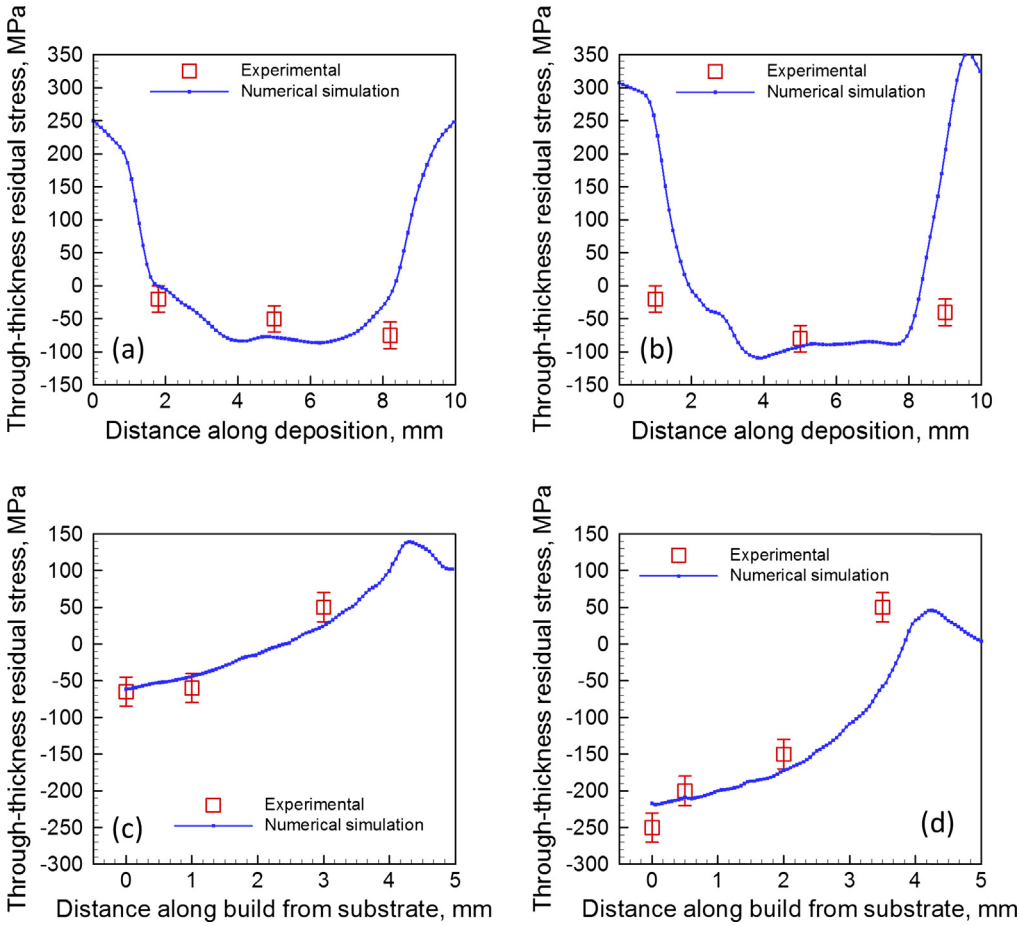

Fig. 4. Comparison between experimentally measured [32] and numerically computed through-thickness residual stress profiles for a 10 layers SS 410 deposit along deposition/travel direction (along line 2) using a laser power of 300 W and scanning speed of (a) 2.5 and (b) 4.2 mm/s and along build direction (along line 5) using a laser power of 600 W and scanning speed of (c) 2.5 and (d) 4.2 mm/s. Other process conditions are given as process parameter set 1 in Table 6.

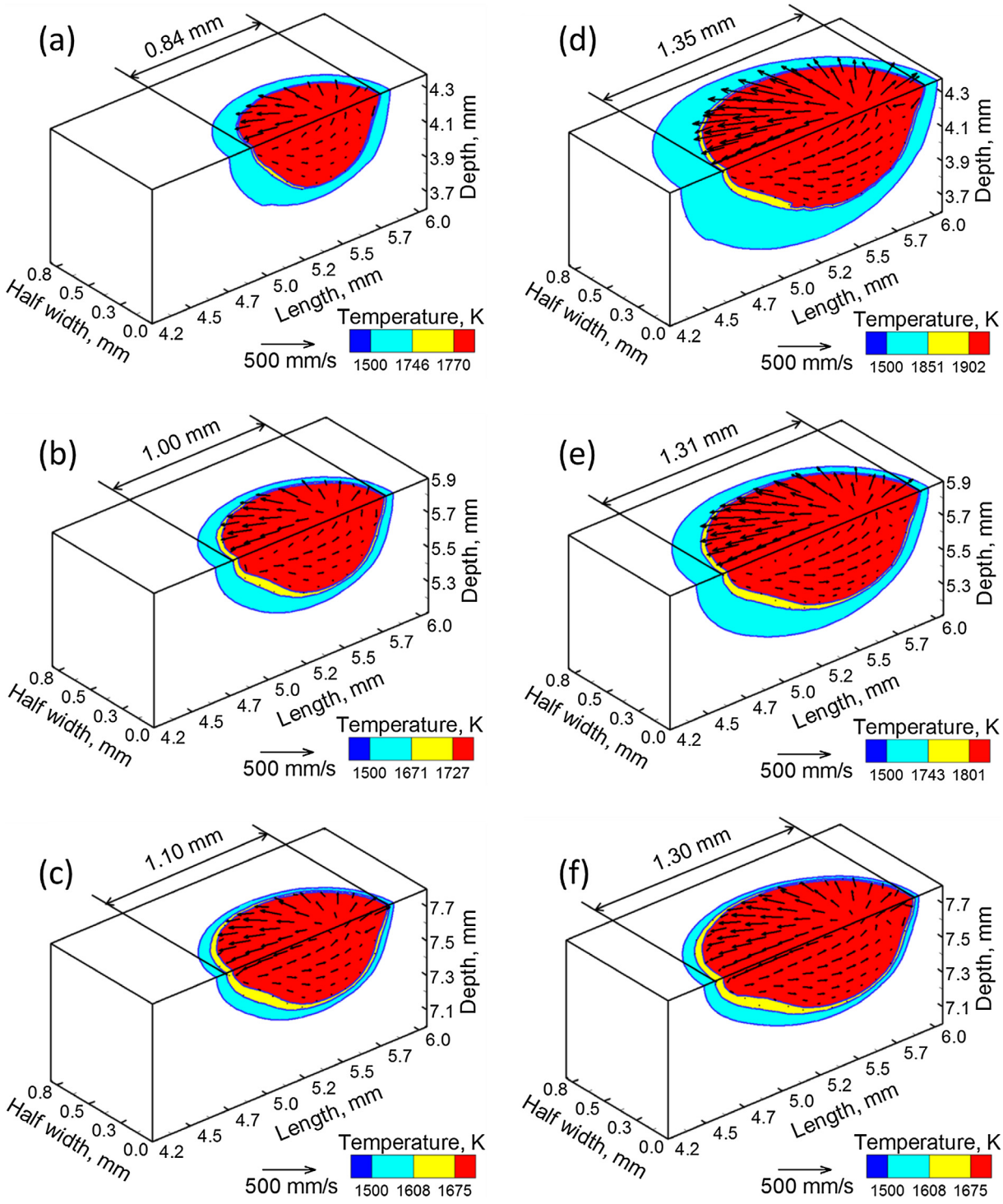

Fig. 5. Temperature and velocity distributions for 2.25Cr-1Mo steel to 800H joint during the deposition of (a) 1st (b) 5th and (c) 10th layer and for Ti-6Al-4V to 800H joint during the deposition of (d) 1st (e) 5th and (f) 10th layer using process parameter set 2 in Table 6.

$$\varepsilon^* = \frac{\beta \Delta T}{EI} \frac{t\, H^{3/2}}{F_o \sqrt{\rho}} \tag{7}$$

where β and ρ are the volumetric coefficient of thermal expansion and density of the alloy, respectively. ΔT is the maximum rise in temperature during the process, t is the characteristic time and H is the heat input per unit length. E and I are the elastic modulus and moment of inertia of the substrate, the product, EI, is the flexural rigidity of the structure. The Fourier number, F_o is the ratio of heat dissipation rate to heat storage rate [33]. The Fourier number and the maximum temperature rise are calculated using the heat transfer and fluid flow model. In 2.25Cr-1Mo steel to 800H joint, pool size increases with layers, as shown in Fig. 5(a)–(c). A large molten pool shrinks more during solidification and results in higher distortion. Therefore, in 2.25Cr-1Mo steel to 800H joint, the strain parameter, a measure of the peak thermal strain, increases with layers as shown in Fig. 6. In Ti-6Al-4V to 800H joint, the molten pool size does not change significantly with layers, as shown in Fig. 5

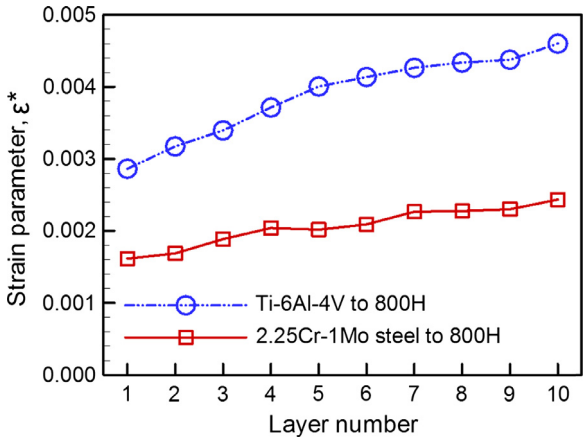

Fig. 6. Variation of strain parameter with number of layer for both 2.25Cr-1Mo steel to 800H and Ti-6Al-4V to 800H joints for the process parameter set 2 in Table 6.

(d)–(f). However, the volumetric thermal expansion coefficient of 800H is almost twice of that of Ti-6Al-4V. Therefore, also in Ti-6Al-4V to 800H joint, the strain parameter increases with layers, as shown in Fig. 6.

Fig. 7 shows the longitudinal stress distribution at the end of 2nd and 10th layer depositions. Longitudinal stress is the component of the residual stress along the scanning direction (x-direction). The positive and the negative values of the stresses in the figures represent the tensile and the compressive residual stresses, respectively. Two important observations can be made from these figures.

1. Magnitudes of the residual stresses vary with the progress of the deposition process. For example, at the end of the deposition of the 2nd layer, the highest magnitude of the longitudinal residual stress is observed near the 2nd layer (see Fig. 7 (a) and (b)). However, with the progress of the deposition process this high residual stress near the 2nd layer is partially alleviated.
2. The residual stresses are spatially non-uniform depending on the varying material properties of the graded joints. For example, Fig. 7(c) and (d) show that after deposition of all 10 layers, the maximum value of the longitudinal stress is near the top of the deposit for both types of joints. However, in Ti-6Al-4V to 800H joint, a high accumulation of tensile residual stress is also observed near the substrate deposit interface.

Figs. 8 and 9 provide detailed explanations of these two observations, respectively. During AM, the previously deposited layers experience reheating and cooling during the deposition of upper layers [21]. Fig. 8(a) and (b) shows the temperature variation with time at Point A (at mid-length of line 1, see Fig. 3) during the fabrication of 2.25Cr-1Mo to 800H joint and Ti-6Al-4V to 800H joint, respectively. Ti-6Al-4V substrate has lower thermal conductivity than 2.25Cr-1Mo steel substrate (Table 1). Therefore, in Ti-6Al-4V to 800H joint, less heat can be transferred through the Ti-6Al-4V substrate. That is why the peak temperatures monitored in Fig. 8 (b) are higher than those in Fig. 8(a) for the same layer. This repetitive heating and cooling partially alleviate the residual stresses for both types of the joints. Fig. 8(c) and (d) shows the longitudinal stress distribution along line 1 (see Fig. 3) after the deposition of 1st, 3rd, 6th and 10th layers, for 2.25Cr-1Mo to 800H joint and Ti-6Al-4V to 800H joint, respectively. For both types of the joints, the magnitude of the residual stress near the center along line 1

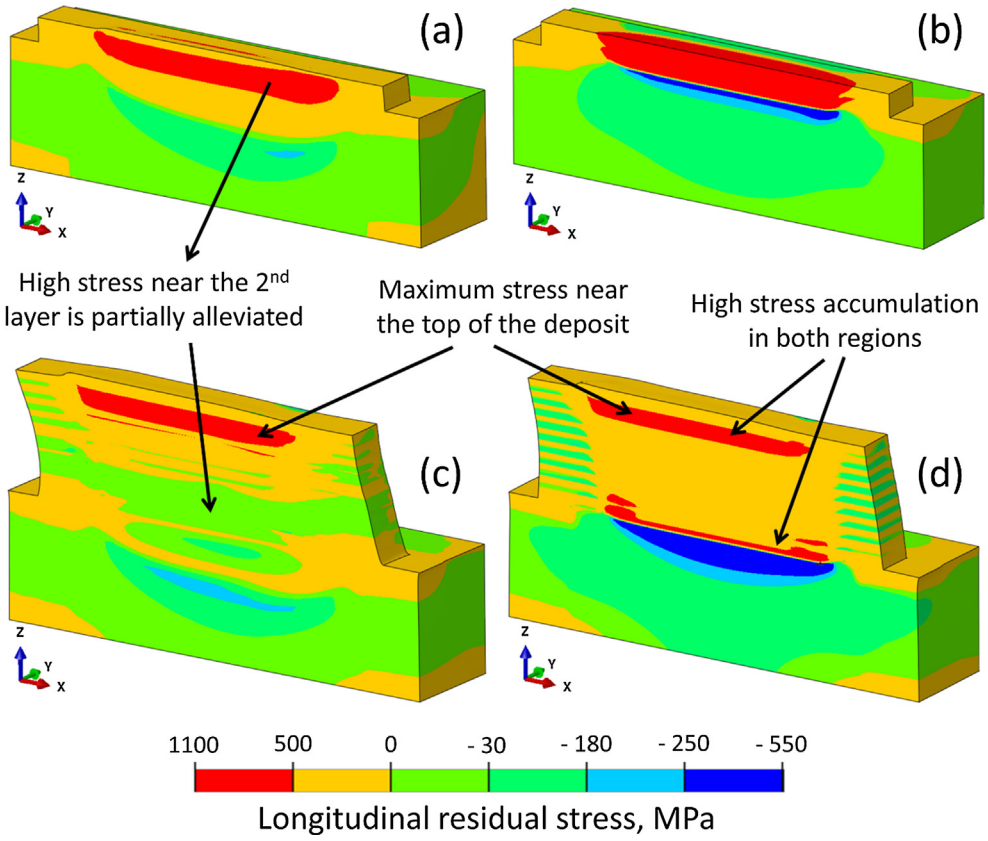

Fig. 7. Longitudinal residual stress (σ_x) distribution at the end of 2nd layer for (a) 2.25Cr-1Mo steel to 800H and (b) Ti-6Al-4V to 800H joints and at the end of 10th layer for (c) 2.25Cr-1Mo steel to 800H and (d) Ti-6Al-4V to 800H joints using process parameter set 2 in Table 6. Scanning direction is along the positive x-axis.

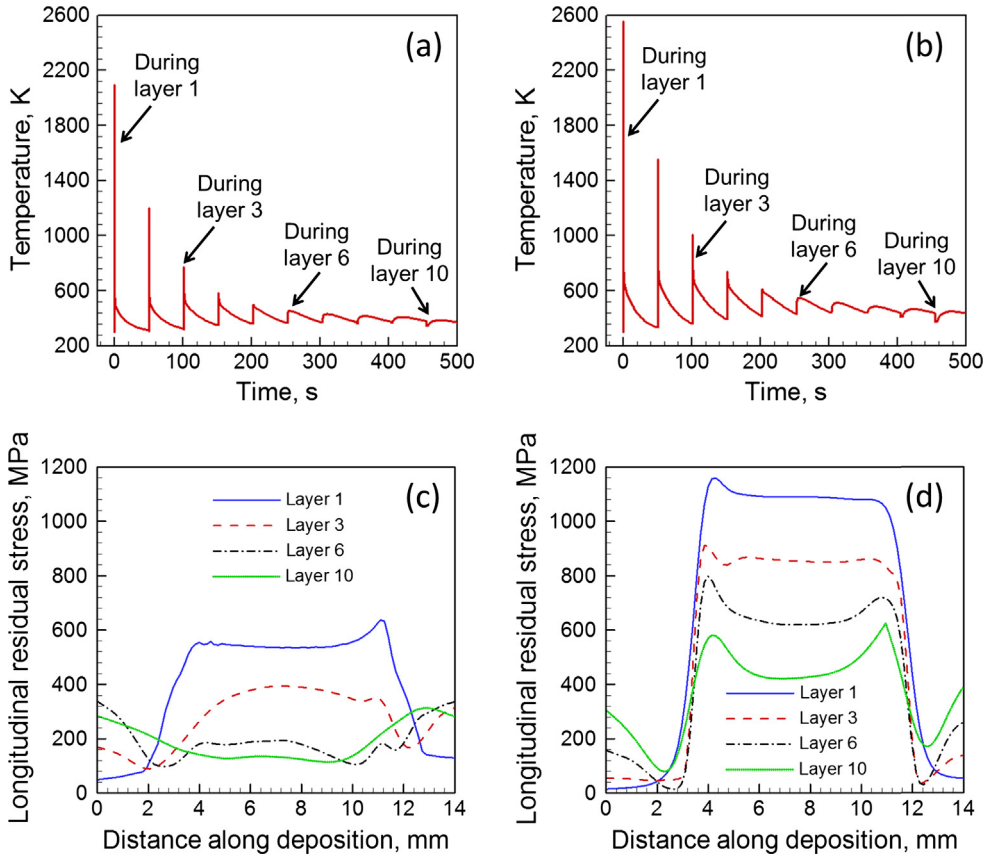

Fig. 8. Variation of the temperature with time monitored at 'point A' (Fig. 3) for (a) 2.25Cr-1Mo steel to 800H and (b) Ti-6Al-4V to 800H joints. Longitudinal residual stress distribution along 'line 1' (Fig. 3) for (c) 2.25Cr-1Mo steel to 800H and (d) Ti-6Al-4V to 800H joints after the deposition of 1st, 3rd, 6th and 10th layer. All results are for the process parameter set 2 in Table 6.

(shown in Fig. 3) decreases with the progress of the deposition process due to the repetitive heating and cooling. However, longitudinal residual stress along line 1 in Ti-6Al-4V to 800 H joint is always higher than that in 2.25Cr-1Mo to 800H joint, due to higher room temperature yield strength and lower thermal expansion coefficient of Ti-6Al-4V substrate compared to those of 2.25Cr-1Mo steel substrate.

In a compositionally graded joint, the residual stresses are spatially non-uniform depending on the local thermo-physical and mechanical properties. Fig. 9(a) and (b) represent the longitudinal residual stress distributions along three lines (line 1, 3 and 4 shown in Fig. 3) for 2.25Cr-1Mo to 800H joint and Ti-6Al-4V to 800H joint, respectively. For 'line 1', only the residual stress along the length of the deposit (12 mm) is plotted to compare the stress profiles inside the deposit. These residual stresses are plotted at the end of the deposition of the 10th layer when the part cools down to the room temperature. 'Line 4' is near the top free end of the wall and cools down to room temperature at the very end. That is why the residual stress along 'line 4' is the highest. Magnitude of the residual stress decreases with the distance from the free end (i.e. moving toward substrate). That is why longitudinal stresses along 'line 1' and 'line 3' are less than that along 'line 4'. However, in Ti-6Al-4V to 800H joint (Fig. 9b), room temperature yield strength near 'line 1' is significantly higher than that along 'line 3' (see Supplementary document for material properties). Therefore, longitudinal stress along 'line 1' is higher than that along 'line 3', as shown in Fig. 9(b). Because of that, in Ti-6Al-4V to 800H joint, large longitudinal residual stresses accumulate both near the top free end (line 4) as well as at the substrate deposit interface (line 1), as shown in Fig. 7(d).

Susceptibility to warping, buckling and delamination depends not only on the magnitude of the residual stresses but also the local room temperature yield strength of the graded joint [18]. Therefore, a normalized residual stress expressed as the ratio of the longitudinal residual stress to the local room temperature yield strength is used for assessment of such problems [18,36]. For 2.25Cr-1Mo to 800H joint (Fig. 9(c)), the normalized residual stresses follow the similar distribution as the longitudinal residual stress (Fig. 9(a)) since the room temperature yield strength does not change significantly along the height of the joint (see Supplementary document for material properties). However, for the Ti-6Al-4V to 800H joint (Fig. 9(d)), due to the higher room temperature yield strength near 'line 1' than that near 'line 3', the values of normalized stresses along 'line 1' and 'line 3' are nearly identical. Therefore, even if the magnitude of the residual stress along 'line 1' is higher than that along 'line 3', the susceptibilities to warping and delamination along these two lines are similar.

Fig. 10 shows the three-dimensional distribution of through-thickness component (along the build direction, σ_z, shown in Fig. 3) of the residual stress for the two types of the graded joints after the deposition of 2nd layer (Fig. 10(a) and (b)) and 10th layer (Fig. 10(c) and (d)). At the end of the deposition process, the top free end of the deposit cools down to the room temperature at the very end. Because of that, tensile stress accumulates near the top free end. That results in the accumulation of large compressive stress near the substrate-deposit interface. The magnitude of the compressive stress at the substrate-deposit interface is maximum at the mid-length of the deposit and the stress quickly transitions into high tensile stress at the two ends. This non-uniformity may result in detachment of the component from the substrate [18].

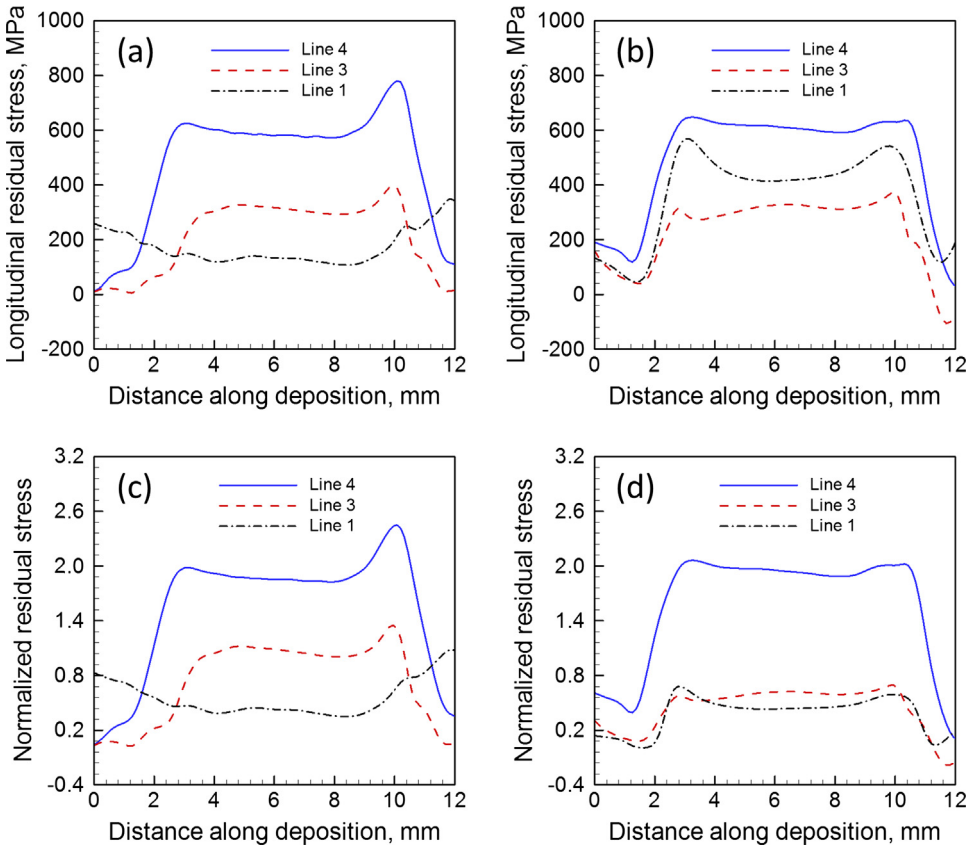

Fig. 9. Longitudinal residual stress distributions for (a) 2.25Cr-1Mo steel to 800H and (b) Ti-6Al-4V to 800H joints and normalized residual stress distributions for (c) 2.25Cr-1Mo steel to 800H and (d) Ti-6Al-4V to 800H joints along 'line 1', 'line 3' and 'line 4' (Fig. 3) at the end of 10 layers deposition when the component cools down to the room temperature. All results are for the process parameter set 2 in Table 6.

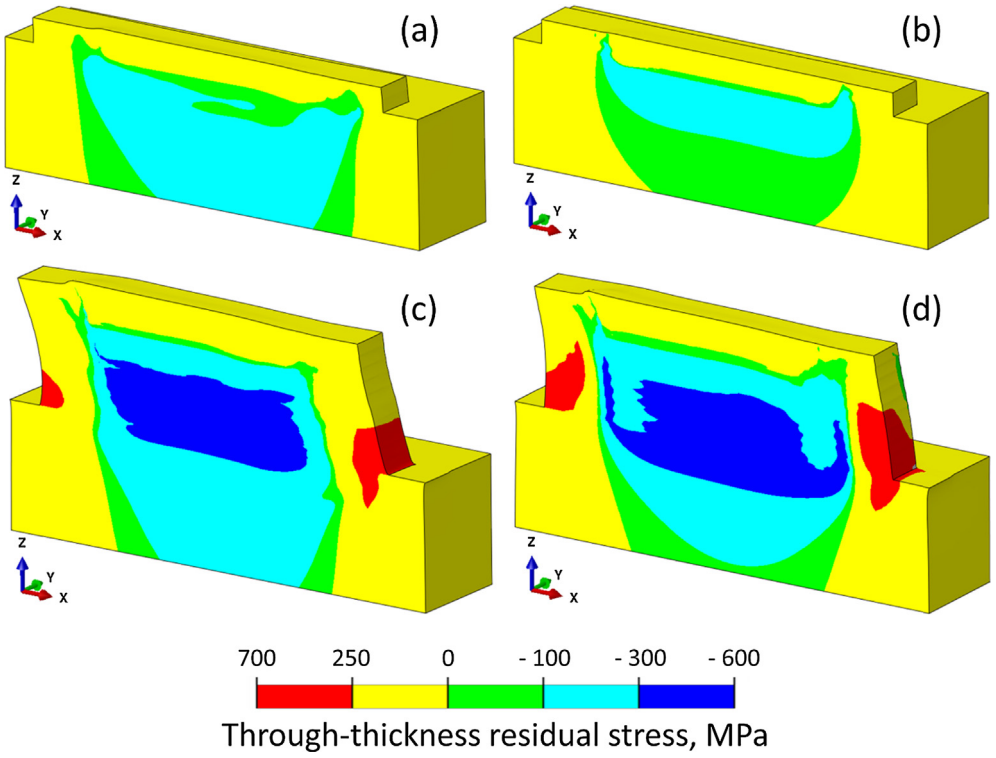

Fig. 10. Through-thickness residual stress distribution at the end of 2nd layer for (a) 2.25Cr-1Mo steel to 800H and (b) Ti-6Al-4V to 800H joints and at the end of 10th layer for (c) 2.25Cr-1Mo steel to 800H and (d) Ti-6Al-4V to 800H joints using process parameter set 2 in Table 6. Scanning direction is along the positive x-axis.

3.4. Graded joints versus dissimilar joints

Fig. 11 explains the benefits of fabricating graded joints over dissimilar joints for minimizing residual stresses and distortion. The results for 2.25Cr-1Mo to 800H joint and Ti-6Al-4V to 800H joint are shown in Fig. 11(a)–(c) and (d)–(f), respectively. In graded joints, the substrate is Ti-6Al-4V or 2.25Cr-1Mo steel and the 10th layer is 800 H, as described before. From the 1st to 9th layer the composition changes with a step of 10 wt% of 800H. On the other hand, for the dissimilar joints, substrate and layer 1 to layer 5 are made of Ti-6Al-4V or 2.25Cr-1Mo steel and 6th to 10th layer are made of 800H, as shown in Fig. 2. Therefore, sharp change in composition occurs at the interface of 5th and 6th layer of the dissimilar joints. All plots in Fig. 11 are made after the end of 10 layers deposition when the component cools down to the room temperature. Longitudinal residual stresses are plotted along the 'line 1' for the entire length of the substrate (14 mm) and through-thickness residual stress and strain are plotted along 'line 5'. Lines 1 and 5 show the entire transition of stresses from substrate to deposit along the laser travel and build height directions, respectively.

The mechanical properties of 2.25Cr-1Mo steel and alloy 800H are similar (see Tables 3 and 5). As a result, no sharp changes in residual stresses and strain at the joint interface are observed. Therefore, graded joint between these two alloys provides marginal benefit over the dissimilar joint for minimizing residual stress

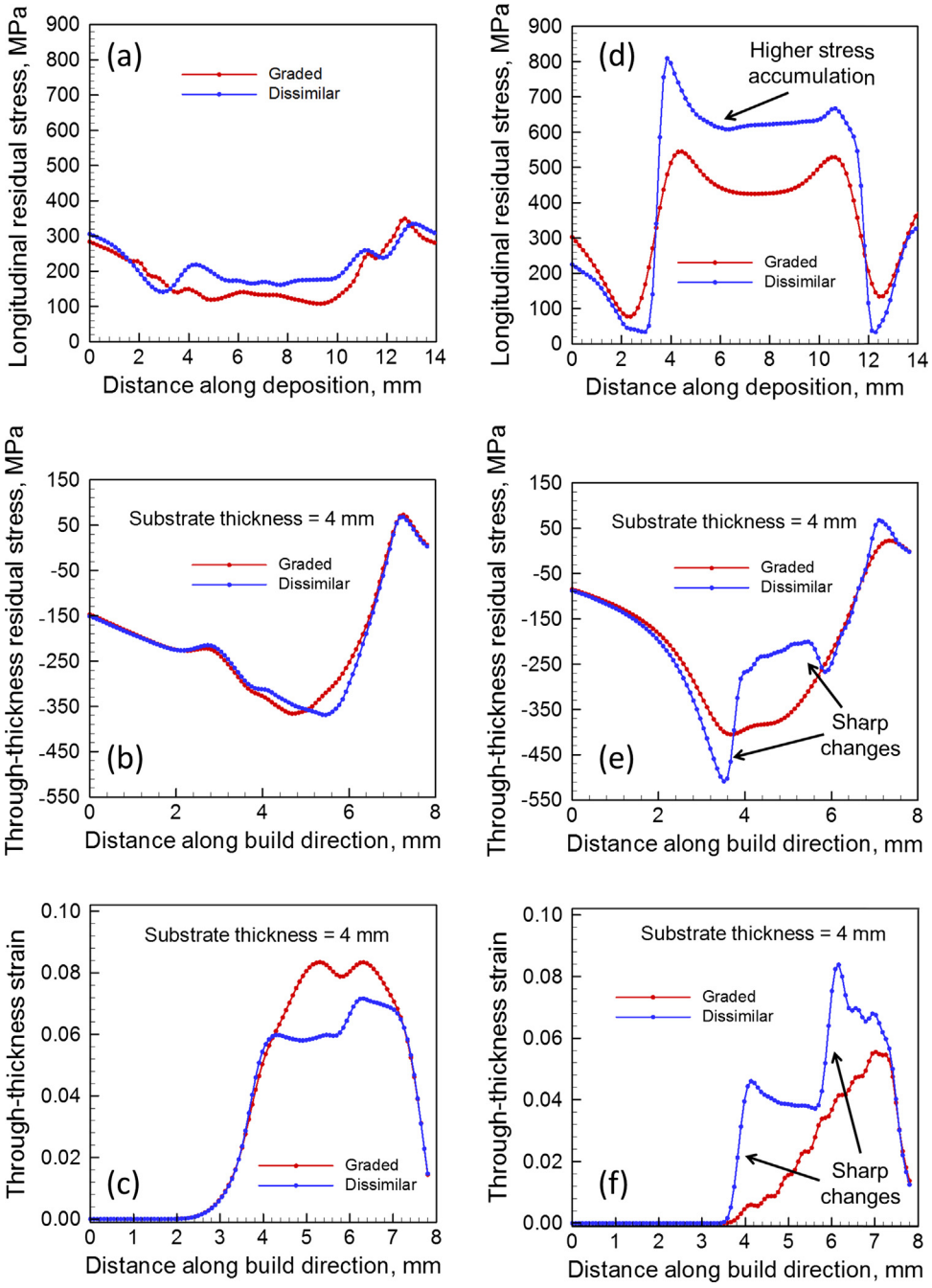

Fig. 11. (a) Longitudinal residual stress along 'line 1', through-thickness (b) stress and (c) strain along 'line 5' for 2.25Cr-1Mo steel to 800H joint and (d) longitudinal residual stress along 'line 1', through-thickness (e) stress and (f) strain along 'line 5' Ti-6Al-4V to 800H joints using process parameter set 2 in Table 6.

and distortion in this pair of dissimilar metals. However, mechanical properties of Ti-6Al-4V are significantly different from those of alloy 800H (see Tables 4 and 5). For example, room temperature yield strength of Ti-6Al-4V is about four times higher than that of 800H. However, room temperature Young's modulus and volumetric expansion coefficient of Ti-6Al-4V are almost half of 800H. Sharp changes in residual stresses and strain in the dissimilar joints due to these differences in mechanical properties can be minimized by fabrication of compositionally graded joints between these two alloys, as shown in Fig. 11(d)–(f). These findings are consistent with the observations made by Williamson et al. [37] where, sharp changes in residual stresses were minimized by fabricating graded joints between pure nickel and alumina by powder metallurgy process.

4. Summary and conclusions

A thermo-mechanical model is developed, validated and utilized to predict residual stresses and distortion based on the accurate temperature field calculated using a well tested heat transfer and fluid flow model and temperature and composition dependent alloy properties estimated using thermodynamic calculations. Residual stresses and distortion are calculated and compared for both compositionally graded as well as dissimilar alloy joints of 2.25Cr-1Mo steel to alloy 800H and Ti-6Al-4V to 800H. The main findings are indicated below.

1. Since, the mechanical properties of Ti-6Al-4V and 800H are significantly different, dissimilar joints between these two alloys exhibited sharp changes in residual stresses and strains at the interface between the two alloys. These sharp changes in residual stresses and strains have been proved to minimize by fabricating a graded joint between these two alloys.
2. Because of the similar mechanical properties of 2.25Cr-1Mo steel and 800H, graded joints between these two alloys provided relatively lower benefits for minimizing residual stresses and distortion compared to the dissimilar joints between them.
3. Residual stresses near the substrate-deposit interface were partially alleviated due to the reheating and cooling during the deposition of the upper layers for all cases studied. However, longitudinal residual stress near the substrate-deposit interface in Ti-6Al-4V to 800H joints was higher than that for 2.25Cr-1Mo steel to 800H joints. This behavior is consistent with the higher room temperature yield strength and lower thermal expansion coefficient of Ti-6Al-4V substrate than 2.25Cr-1Mo steel substrate.
4. The computed ratio of the longitudinal residual stress at the substrate-deposit interface to the room temperature yield strength of the substrate provided information about the susceptibilities to warping, buckling and detachment of deposit from its substrate. A graded joint between 800H and Ti-6Al-4V on Ti-6Al-4V substrate was less susceptible to these defects than a joint between 800H and 2.25Cr-1Mo steel on 2.25Cr-1Mo steel substrate because of the higher room temperature yield strength of the Ti-6Al-4V substrate than 2.25Cr-1Mo steel.
5. The thermal strain during deposition increases with layers for both graded joints of Ti-6Al-4V to 800H and 2.25Cr-1Mo steel to 800H. For the former, this is mainly because of the increasing heat accumulation during the deposition of upper layers. For the latter, the rising strain results largely from the increase in volumetric expansion coefficient as more 800H is added into Ti-6Al-4V in the upper layers. Moreover, for a particular layer, the value of the strain for Ti-6Al-4V to 800H joint is higher than that for 2.25Cr-1Mo steel to 800H joint mainly due to the low elastic modulus and density of the Ti-6Al-4V substrate.

Acknowledgement

We acknowledge the support from US Department of Energy NEUP Grant [DE-NE0008280]. One of the authors (T.M.) also acknowledges the support from American Welding Society research fellowship grant [179466]. Finally, W.Z. acknowledges the support from US Department of Energy NEUP Grant [DE-NE0000708].

Appendix A. Supplementary material

Supplementary data associated with this article can be found, in the online version, at https://doi.org/10.1016/j.commatsci.2017.11.026.

References

[1] C.D. Lundin, Dissimilar metal welds-transition joints literature review, Weld. J. 61 (2) (1982) 58–63.
[2] D. Deng, K. Ogawa, S. Kiyoshima, N. Yanagida, K. Saito, Prediction of residual stresses in a dissimilar metal welded pipe with considering cladding, buttering and post weld heat treatment, Comput. Mater. Sci. 47 (2009) 398–408.
[3] Z. Zeng, X. Li, Y. Miao, G. Wu, Z. Zhao, Numerical and experiment analysis of residual stress on magnesium alloy and steel butt joint by hybrid laser-TIG welding, Comput. Mater. Sci. 50 (5) (2011) 1763–1769.
[4] D. Delfosse, N. Cherradi, B. Ilschner, Numerical and experimental determination of residual stresses in graded materials, Compos. Part B: Eng. 28 (1-2) (1997) 127–141.
[5] D. Qiao, W. Zhang, T.Y. Pan, P. Crooker, S.A. David, Z. Feng, Evaluation of residual plastic strain distribution in dissimilar metal weld by hardness mapping, Sci. Technol. Weld Join. 18 (7) (2013) 624–630.
[6] G.J. Brentrup, J.N. DuPont, Fabrication and characterization of graded transition joints for welding dissimilar alloys, Weld. J. 92 (2013) 72–79.
[7] T. DebRoy, H.L. Wei, J.S. Zuback, T. Mukherjee, J.W. Elmer, J.O. Milewski, A.M. Beese, A. Wilson-Heid, A. De, W. Zhang, Additive manufacturing of metallic components – process, structure and properties, Prog. Mater. Sci. 92 (2018) 112–224.
[8] G.K. Lewis, E. Schlienger, Practical considerations and capabilities for laser assisted direct metal deposition, Mater. Des. 21 (4) (2000) 417–423.
[9] A. Reichardt, R.P. Dillon, J.P. Borgonia, A.A. Shapiro, B.W. McEnerney, T. Momose, P. Hosemann, Development and characterization of Ti-6Al-4V to 304L stainless steel gradient components fabricated with laser deposition additive manufacturing, Mater. Des. 104 (2016) 404–413.
[10] A. Hinojos, J. Mireles, A. Reichardt, P. Frigola, P. Hosemann, L.E. Murr, R.B. Wicker, Joining of Inconel 718 and 316 Stainless Steel using electron beam melting additive manufacturing technology, Mater. Des. 94 (2016) 17–27.
[11] B.E. Carroll, R.A. Otis, J.P. Borgonia, J. Suh, R.P. Dillon, A.A. Shapiro, D.C. Hofmann, Z.K. Liu, A.M. Beese, Functionally graded material of 304L stainless steel and Inconel 625 fabricated by directed energy deposition: characterization and thermodynamic modeling, Acta Mater. 108 (2016) 46–54.
[12] L.D. Bobbio, R.A. Otis, J.P. Borgonia, R.P. Dillon, A.A. Shapiro, Z.K. Liu, A.M. Beese, Additive manufacturing of a functionally graded material from Ti-6Al-4V to Invar: experimental characterization and thermodynamic calculations, Acta Mater. 127 (2017) 133–142.
[13] P.H. Chang, T.L. Teng, Numerical and experimental investigations on the residual stresses of the butt-welded joints, Comput. Mater. Sci. 29 (2004) 511–522.
[14] P.J. Withers, H.K.D.H. Bhadeshia, Residual stress. Part 1–Measurement techniques, Mater. Sci. Technol. 17 (4) (2001) 355–365.
[15] Z. Wang, E. Denlinger, P. Michaleris, A.D. Stoica, D. Ma, A.M. Beese, Residual stress mapping in Inconel 625 fabricated through additive manufacturing: Method for neutron diffraction measurements to validate thermomechanical model predictions, Mater. Des. 113 (2017) 169–177.
[16] A.S. Wu, D.W. Brown, M. Kumar, G.F. Gallegos, W.E. King, An experimental investigation into additive manufacturing-induced residual stresses in 316L stainless steel, Metal. Mater. Trans. A 45 (13) (2014) 6260–6270.
[17] W. Zhang, Z. Feng, P. Crooker, Improved procedure for computing residual stresses from neutron diffraction data and its application to multipass dissimilar welds, Sci. Technol. Weld Join. 16 (3) (2011) 254–260.
[18] T. Mukherjee, W. Zhang, T. DebRoy, An improved prediction of residual stresses and distortion in additive manufacturing, Comput. Mater. Sci. 126 (2017) 360–372.
[19] L.E. Svensson, B. Gretoft, H.K.D.H. Bhadeshia, An analysis of cooling curves from the fusion zone of steel weld deposits, Scand. J. Metall. 15 (1986) 97–103.
[20] B.H. Rabin, R.L. Williamson, S.M.R.S. Suresh, Fundamentals of residual stresses in joints between dissimilar materials, MRS Bull. 20 (1) (1995) 37–39.
[21] V. Manvatkar, A. De, T. DebRoy, Heat transfer and material flow during laser assisted multi-layer additive manufacturing, J. Appl. Phys. 116 (12) (2014) 124905.

[22] V. Manvatkar, A. De, T. DebRoy, Spatial variation of melt pool geometry, peak temperature and solidification parameters during laser assisted additive manufacturing process, Mater. Sci. Technol. 31 (8) (2015) 924–930.
[23] G.L. Knapp, T. Mukherjee, J.S. Zuback, H.L. Wei, T.A. Palmer, A. De, T. DebRoy, Building blocks for a digital twin of additive manufacturing, Acta Mater. 135 (2017) 390–399.
[24] Abaqus Documentation, Version 6.14, Dassault Systems, 2015.
[25] N. Saunders, Z. Guo, X. Li, A.P. Miodownik, J.P. Schille, Using JMatPro to model materials properties and behavior, JOM 55 (12) (2003) 60–65.
[26] N. Saunders, A.P. Miodownik, CALPHAD: A comprehensive guide, vol. 1, Elsevier, 1998.
[27] N. Saunders, Z. Guo, X. Li, A.P. Miodownik, J.P. Schille, Modelling the material properties and behavior of Ni-based superalloys, Superalloys (2004) 849–858.
[28] Z. Fan, P. Tsakiropoulos, A.P. Miodownik, A generalized law of mixtures, J. Mater. Sci. 29 (1994) 141–150.
[29] A. Raghavan, H.L. Wei, T.A. Palmer, T. DebRoy, Heat transfer and fluid flow in additive manufacturing, J. Laser Appl. 25 (5) (2013) 052006.
[30] T. DebRoy, S.A. David, Physical processes in fusion welding, Rev. Mod. Phys. 67 (1) (1995) 85.
[31] Y.S. Lee, W. Zhang, Modeling of heat transfer, fluid flow and solidification microstructure of nickel-base superalloy fabricated by laser powder bed fusion, Addit. Manufact. 12 (2016) 178–188.
[32] L. Wang, S.D. Felicelli, P. Pratt, Residual stresses in LENS-deposited AISI 410 stainless steel plates, Mater. Sci. Eng. A 496 (1) (2008) 234–241.
[33] T. Mukherjee, V. Manvatkar, A. De, T. DebRoy, Dimensionless numbers in additive manufacturing, J. Appl. Phys. 121 (6) (2017) 064904.
[34] T. Mukherjee, J.S. Zuback, A. De, T. DebRoy, Printability of alloys for additive manufacturing, Sci. Rep. 6 (2016).
[35] T. Mukherjee, V. Manvatkar, A. De, T. DebRoy, Mitigation of thermal distortion during additive manufacturing, Scripta Mater. 127 (2017) 79–83.
[36] R. Jackson, I. Chusoipin, I. Green, A finite element study of the residual stress and deformation in hemispherical contacts, Trans. ASME J. Tribol. 127 (3) (2005) 484–493.
[37] R.L. Williamson, B.H. Rabin, J.T. Drake, Finite element analysis of thermal residual stresses at graded ceramic-metal interfaces. Part I. Model description and geometrical effects, J. Appl. Phys. 74 (2) (1993) 1310–1320.